THE JOURNAL OF PHYSICAL CHEMISTRY C
A JOURNAL OF THE AMERICAN CHEMICAL SOCIETY

pubs.acs.org/JPCC

Article

Subsurface Characteristics of Metal-Halide Perovskites Polished by an Argon Ion Beam

Yu-Lin Hsu, Chongwen Li, Andrew C. Jones, Michael T. Pettes, Ashif Chowdhury, Yanfa Yan, and Heayoung P. Yoon*

Cite This: J. Phys. Chem. C 2023, 127, 7461−7470

Read Online

ACCESS | Metrics & More | Article Recommendations | Supporting Information

ABSTRACT: Focused ion beam (FIB) techniques have been frequently used to section metal-halide perovskites for microstructural investigations. However, the ion beams directly irradiating the sample surface may alter its properties far different from those of pristine, potentially leading to modified deterioration mechanisms under aging stressors. Here, we combine complementary approaches to measure the subsurface characteristics of polished perovskites and identify the chemical species responsible for the measured properties. Analysis of the experimental results in conjunction with Monte Carlo simulations indicates that atomic displacements and local heating occur in the first ≈15 nm of the subsurface of methylammonium lead iodide ($MAPbI_3$) by glancing-angle Ar^+ beam irradiation (4 kV at 3°). The lead-rich, iodine-deficient surface promotes rapid phase segregation under thermal aging conditions. On the other hand, despite the subsurface modification, our experiments confirm that the rest of the $MAPbI_3$ bulk retains the material integrity. Our observation supports that polished perovskites could serve in studying the properties of bulk or buried junctions far away from the altered subsurface with care.

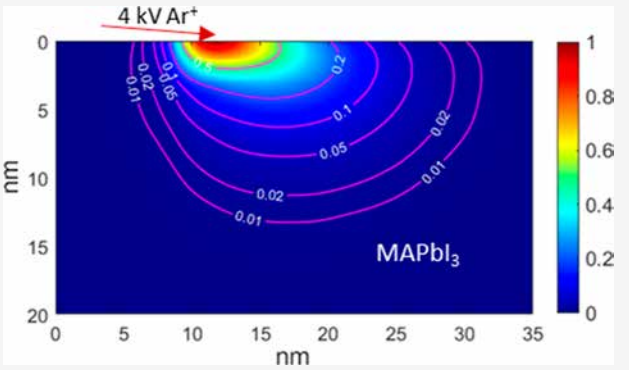

1. INTRODUCTION

Ion-beam-based sample preparation techniques have been extensively used in studying the microstructural and interfacial characteristics of thin-film solar cells. Compared to traditional chemical and mechanical polishing, a focused ion beam (FIB) is fast and site-specific, minimizing mechanical damage, such as distorted structures, superficial scratching, and smearing at the surface.[1−3] For example, a liquid metal-ion source (e.g., ^{31}Ga) equipped with a typical dual-beam FIB/SEM (scanning electron microscopy) system produces a ray of ion beam at the accelerating voltage of 5 to 30 kV.[4,5] The focused beam (<10 nm beam) irradiated on the target material introduces cascade events, resulting in the etching of the segment of interest. Post-processing methods are often applied to further remove or eliminate beam damage. The practices include low-energy FIB, gas-assisted etching, wet etching, and low-temperature milling.[4,6,7] Previous efforts also demonstrated that a broad argon ion beam (^{18}Ar; ≈1 mm beam) could effectively remove the FIB damage. Giannuzzi et al. showed a damaged region of less than 1 nm on a Si lamella after final thinning with 0.2 kV Ar^+ polishing.[8]

Applications of FIB have enabled measuring the morphology and local optoelectronic responses of metal-halide perovskite devices.[9,10] Smooth sample surfaces are desirable for many atomic/nanoscale measurements due to the scattering of the probe beams that can introduce artifacts arising from the sample topography rather than the characteristics of the sample of interest. Numerous transmission electron microscopy (TEM; beam energy of 80 to 300 keV) studies revealed the structural and compositional characteristics of perovskite solar cells (PSCs) under controlled environmental stressors.[11,12] High-fidelity Kelvin probe force microscopy (KPFM) demonstrated the distinct potential distribution of cross-sectional PSCs under dark and light illumination, which can be correlated to ion migrations and defect dynamics.[13,14] While beneficial, recent publications have reported the beam sensitivity of hybrid organic−inorganic perovskites.[10,15−18] For instance, PSC lamellas in TEM displayed significant deterioration during data acquisition via chemical-bond breakage and local heating. Cathodoluminescence (CL) spectra repeatedly collected on the same area of a FIB-milled $MAPbI_3$ (methylammonium lead iodide) presented the defect formation and irreversible decomposition within a few minutes.[19] Such rapid degradation seems mainly to be caused by high-energy electron beams. It is also possible that the outer layer of the PSC is already altered during the FIB processing, accelerating fast degradation via

Received: December 30, 2022
Revised: March 24, 2023
Published: April 10, 2023

modified mechanisms that may be far different from their pristine devices.

Herein, we thoroughly investigate the subsurface characteristics of perovskites exposed to an irradiating ion beam. We demonstrate glancing-angle Ar^+ milling to produce a smooth surface of $MAPbI_3$ (4 kV at 3°). The optoelectronic characteristics of the polished samples are measured by photoluminescence (PL) and KPFM and compared to their pristine controls. High-resolution X-ray photoemission spectroscopy (XPS) identifies the chemical species responsible for the observed PL and XPS, revealing a lead-rich and iodine-deficient surface induced by ion beams. Analysis of experimental results in conjunction with Monte Carlo simulations indicates that a thin layer of $MAPbI_3$ (≈15 nm) is damaged during the polishing while still retaining the material integrity in the rest of the film. We discuss the implications of our findings to study deterioration mechanisms of perovskites and possible uses of polished samples for surface-insensitive measurements (e.g., two-photon microscopy studying buried junctions).

2. METHODS

2.1. PSC Fabrication. Glass substrates coated with fluorine-doped tin oxide (FTO; a thickness of 200 nm) were cleaned with acetone, isopropyl alcohol (IPA), and deionized (DI) water. The N_2-dried substrates were further cleaned with oxygen (O_2) plasma. A 35 nm SnO_2 (ETL) was deposited on FTO by the atomic layer deposition (ALD) system (Picosun) using high-purity (99.9999%) tetrakis(dimethylamino)tin(IV) and DI water as precursors. $MAPbI_3$ precursor ink was synthesized by mixing 1 mM lead iodide (PbI_2) and 1 mM methylammonium iodide (MAI) in dimethylformamide (DMF) with an additive of 0.02 mM lead bisdicyanoamide ($Pb(SCN)_2$) in dimethyl sulfoxide (DMSO). This $MAPbI_3$ ink was spun coated on ETL at a spin-speed of 500 rpm for 3 s, followed by 4000 rpm for 50 s. During the second spin step (i.e., about 11 s from the first spinning), anti-solvent diethyl ether (720 μL) was dropped onto the center of the sample.[20] The sample was cured on a hotplate at 60 °C for 3 min, followed by 100 °C for 10 min. The samples were stored under N_2 environmental conditions in the dark before Ar^+ polishing and characterizations.

2.2. Glancing-Angle Ar Ion-Beam Polishing. We performed a series of broad Ar^+ milling procedures (Fischione model 1060) to reduce the surface roughness of the $MAPbI_3$ layer. This system is equipped with two ion sources, where the angle can be adjusted from 0 to 10° to the direction parallel to the sample surface. We used a single ion gun irradiating at 3° without rotation in this experiment. High-purity (99.999%) argon gas was used for the ion sources at a base pressure of 3.8×10^{-4} Torr. The beam current was set to ≈50 μA for all samples. Since the Faraday cage measuring the current was located far beyond the sample stage, we used the magnitude of the current only for checking the proper system operation and not for the quantitative estimation of the beam energy delivered to the specimen. $MAPbI_3$ samples were polished by Ar^+ beams (4 kV irradiating at 3°) for 10 min at room temperature.

2.3. Hyperspectroscopy Photoluminescence Microscopy. We used a 224 nm (5.08 eV) UV light source that produced a nominal power of approximately 10 μW on the sample (LEXEL Quantum 8 SHG CW deep UV and tunable visible argon ion laser, Cambridge Laser Laboratories Inc.). The PL emission was collected using a 600 mm^{-1} holographic grating with a 40× (numerical aperture [N. A.] = 0.5) reflective objective lens (LMM40X-UVV, ThorLabs). The confocal hole diameter was set to 300 μm. Point PL spectra were taken by rastering over a 50 μm diameter area using fast scanning mirrors as the mean of two spectra recorded for 0.5 s each. PL mapping was performed at a pixel step of 333 μm in the x- and y-directions. The hyperspectroscopy PL signals were collected on a 50 μm diameter area of each spatial pixel. The focal height was obtained at each real space pixel by optimizing the PL signal in the spectral window (760−770 nm) over a 150 μm height range with 0.25 μm z-axis resolution.

2.4. Kelvin Probe Force Microscopy. KPFM was conducted using a Bruker Dimension Icon atomic force microscope operating in frequency-modulated (FM-KPFM) feedback to determine the surface potential. The work function values of the PSC samples were calculated using the surface potentials of gold (5.1 eV) and highly oriented pyrolytic graphite (HOPG; 4.68 eV). Sample maps were collected with a feedback force setpoint of 8 nN with a scan rate of 0.5 Hz.

2.5. X-ray Photoemission Spectroscopy. XPS measurements were carried out using an Al Kα X-ray source (1.486 KeV; Kratos Axis Ultra DLD). The samples were first placed in a load-lock, pumped down to a vacuum pressure of 1×10^{-7} Torr, and transferred to the analysis chamber ($<6 \times 10^{-10}$ Torr). The polished $MAPbI_3$ sample was immediately transferred to the XPS chamber after the milling, limiting unintentional air exposure. The emission current was 8 mA, and the anode voltage was 15 kV. A typical beam spot size for the XPS was 300 μm × 700 μm. A neutral gun was employed to eliminate the charge effect during the XPS measurement. The XPS signals were acquired with an energy resolution of 1 eV for survey scans and 0.1 eV for high-resolution spectra. The measured spectra were calibrated using the core level peak of C 1s (C−C bonds) at 284.5 eV. Peak fitting and quantitative analysis (e.g., the atomic concentration of each element) were performed using a commercial software with the average matrix relative sensitivity factors (CasaXPS, Origin Pro).

2.6. Thermal Degradation. Qualitative thermal degradation of PSC of Ar^+ polished samples was examined using a heat lamp. We placed a ceramic lamp heater (150 W; a diameter of 7 cm) above the sample stage, equipped with a K-type thermal couple probe. The distance between the top of the sample and the bottom of the lamp was approximately 9 cm, providing relatively uniform heat distribution in the sample stage. When the stage temperature reached the set value (e.g., 150 °C), we located Ar^+-polished and control samples in proximity under the lamp. A series of pictures were taken at a few minute intervals for an hour until the samples were fully degraded and turned color from dark brown to yellow (e.g., PbI_2).

2.7. Monte Carlo Simulations. We performed Monte Carlo simulations using a software package to study the Ar^+ beam interaction with metal-halide perovskites (SRIM/TRIM: stopping and range of ions in matter/transport and range of ions in matter). SRIM/TRIM covers multiple inelastic collisions, and it models range, damage, recoils, thermal effects, and sputtering. The standard TRIM database was used to set the simulation configuration. The injected ion data were set to Ar (atomic number of 18 and atomic mass of 39.962 u), whereas a 500 nm-thick $MAPbI_3$ was set to the target material (a density of 4.16 g/cm^3).[21] The standard values of the atomic number, atomic weight, displacement energy, lattice energy, and surface energy for each component of $MAPbI_3$ were followed in the TRIM library without modification. Our model used 200,000 ions for each simulation. The extracted 2D/3D raw datasets were analyzed using MATLAB.

https://doi.org/10.1021/acs.jpcc.2c09122
J. Phys. Chem. C 2023, 127, 7461−7470

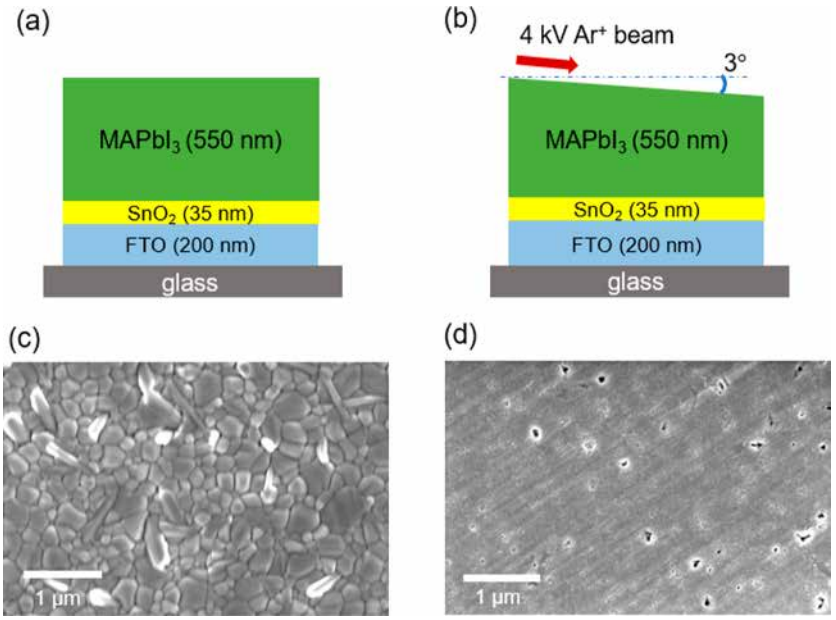

Figure 1. Schematics of methylammonium lead iodide ($MAPbI_3$) samples: (a) pristine and (b) polished using Ar^+ beams. Representative SEM images of $MAPbI_3$ (c) pristine and (d) polished samples.

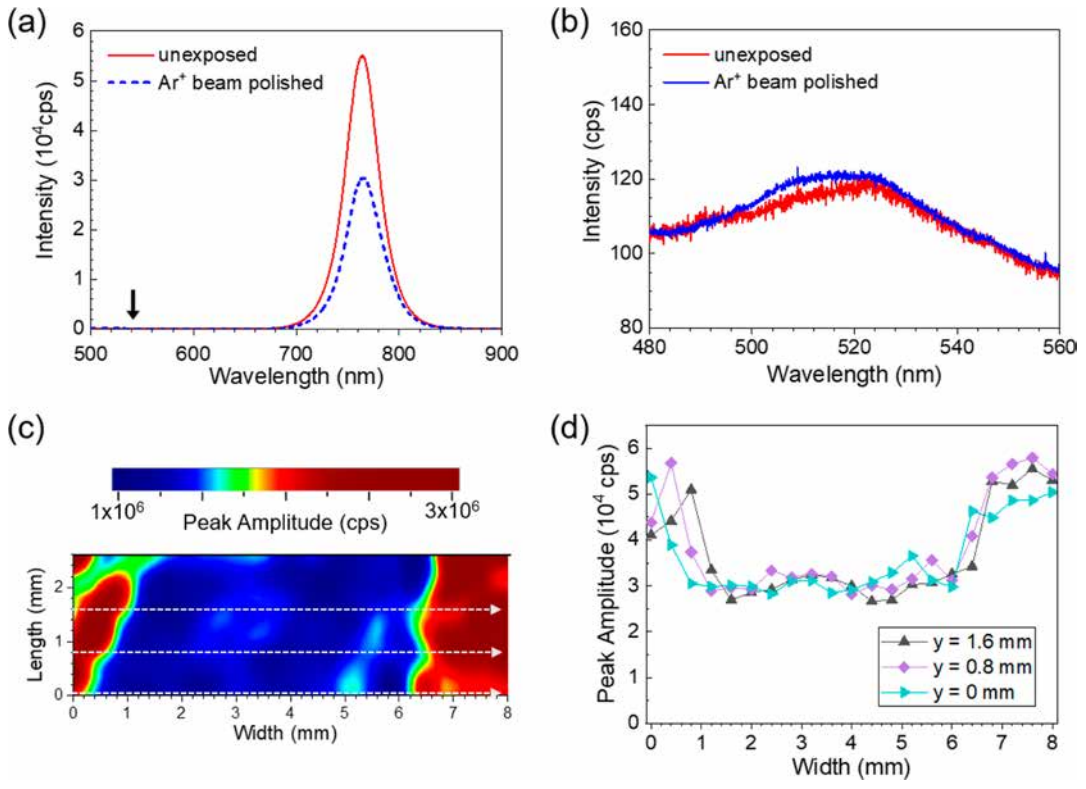

Figure 2. (a) PL responses of pristine and polished samples. The prominent peak 765 nm (1.62 eV) is associated with the band gap emission. PL region near 500 nm (marked with an arrow in black) is replotted in (b). The wavelength 516 nm corresponds to the 2.4 eV band gap of PbI_2. (c) PL map plotted with the peak intensities at 765 nm. The center area (in blue) was exposed to the Ar^+ beam, showing a lower PL intensity. The other regions (in red) were not exposed to the ion beam. (d) Intensity profiles along the width of the sample at the length of 0, 8, and 1.6 mm [see white arrows in (c)].

3. RESULTS AND DISCUSSION

Our typical PSC consists of an $MAPbI_3$ film sandwiched between an electron transfer layer (ETL) and a hole transfer layer (HTL). A FTO front contact on ETL and an Au back contact on HTL were used for photovoltaic measurements. In this study, we excluded the HTL and the Au contact to understand the direct impact of the Ar^+ beam on $MAPbI_3$. Figure 1a illustrates the configuration of the sample: glass/FTO (200 nm)/SnO_2 (35 nm)/$MAPbI_3$ (550 nm). We applied Ar^+ beams to section the top surface of $MAPbI_3$. At an acceleration voltage of 4 kV, the broad beam (spot size >1 mm) was irradiated at an incident angle of 3° parallel to the sample surface

https://doi.org/10.1021/acs.jpcc.2c09122
J. Phys. Chem. C 2023, 127, 7461−7470

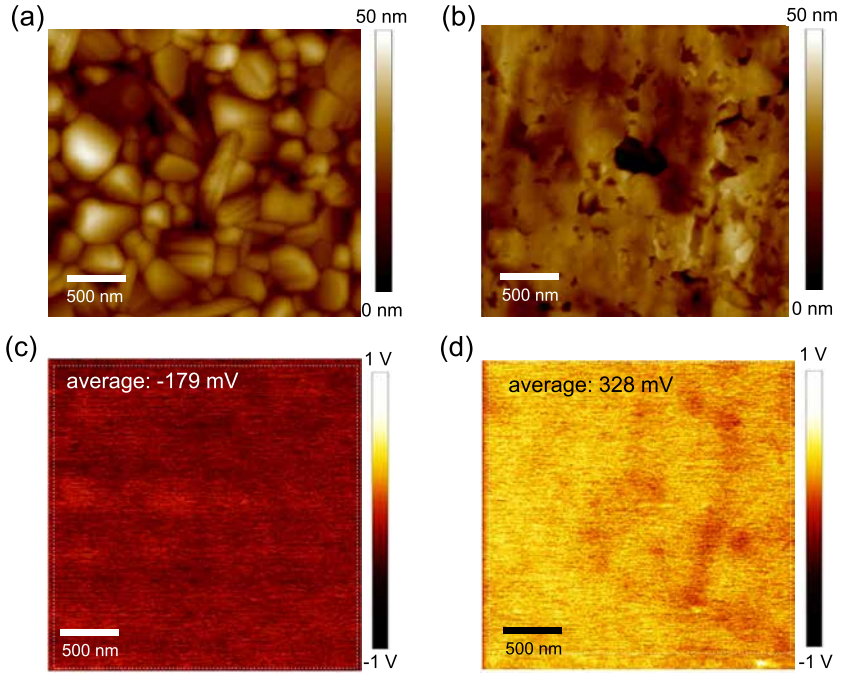

Figure 3. Topography of $MAPbI_3$ obtained using AFM of (a) pristine and (b) polished samples. The peak-to-valley surface roughness reduces from 100 to 10 nm with the polishing processes. (c,d) CPD simultaneously collected with the AFM images in (a,b). The average CPD of the pristine surface (−179 mV ± 150 mV) increases to 328 mV ± 150 mV after polishing.

(Figure 1b). The polishing process was performed for 10 min at room temperature. By setting the beam focus to 0%, the initial beam injected on the edge of the sample was widely spread on the sample surface in a trapezoidal shape. We characterized both polished and unpolished areas of the same sample along with an unexposed pristine perovskite sample. Figure 1c,d shows representative SEM images of $MAPbI_3$ "before" and "after" the polishing. A typical grain size of the pristine sample ranged from 100 to 500 nm (Figure 1c). As seen in Figure 1d, the glancing-angle Ar^+ beam effectively removed the sample roughness but did not appreciably affect the film thickness. The porous structures near grain boundaries and the pinholes seen on the milled area are likely attributed to the grain growth during the thermal annealing after spin-coating of PSC precursors.[22]

The primary focus in the present report is to analyze the subsurface characteristics rather than individual microstructural assessments. Luminescence characteristics were measured using PL spectroscopy at a laser beam excitation of 244 nm. At a nominal beam size of ≈ (400 μm),[2] the laser power was set to ≈10 μW to reduce possible light degradation during the measurements. We used FDTD (finite-difference time-domain) simulations to obtain the absorption profile in $MAPbI_3$ under 244 nm illumination by using the refractive indices extracted from an ellipsometry study.[23−25] The simulation results suggest the illuminated photons (λ = 244 nm) are mainly absorbed within the subsurface of <100 nm, indicating the PL probe can be sensitive to subsurface modification. Details of the simulation can be found in the Supporting Information section.

Figure 2a,b displays the representative PL spectra collected on the polished region compared to the unexposed area. The prominent peak at 765 nm (1.62 eV) in Figure 2a corresponds to the band gap of $MAPbI_3$, showing an excellent agreement with the previous studies.[26,27] This band gap emission decreases by 40% after the milling, but the overall intensity is still strong. In recent literature, Kosasih et al. reported a band gap emission on a FIB-prepared $MAPbI_3$ lamella (8 kV Ga^+ beam) using CL, where the peak near 1.6 eV was blue-shifted and broadened (≈0.2 eV) compared to their bulk controls.[19] The authors suggested that this behavior could be linked to the mechanical stress causing suppression of the atomic orbital overlap and an amorphization of $MAPbI_3$. In contrast, our PL peak position of 1.62 eV and the full-width at half-maximum (FWHM) of 0.09 eV remain unchanged after Ar^+ beam polishing. The weak peaks at 517 nm (2.4 eV) correspond to the PbI_2, indicating that ion beams might degrade a small portion of the surface. The consistent PL characteristic was observed across the large area of the Ar^+-milled sample. Figure 2c shows a PL intensity map collected in an area of 8 mm × 2.6 mm at a step size of 800 μm. The color contrast reflects the peak height at 1.62 eV (765 nm). Uniform and strong PL responses are apparent in the unmilled regions (in red), whereas the Ar^+ polished region shows relatively lower PL intensities (in blue). Figure 2d plots the magnitudes of the PL height extracted from three lines marked in Figure 2c. The high luminescence obtained on the unexposed area (x < 1 mm, x > 6 mm; ≈5 × 10^4 counts per second [cps]) reduced to approximately 40% in the center (1 mm < x < 6 mm; ≈3 × 10^4 cps), where the Ar ion beam was irradiated. The FWHM of all PL spectra ranges within a little variation (<0.01 eV) and does not show any significant peak broadening across the sample. The overall PL intensity after the milling is still strong, which implies that the integrity of the bulk $MAPbI_3$ is preserved.

We examine the electrostatics of the $MAPbI_3$ surface after Ar^+ milling using KPFM that measures the contact potential difference (CPD; V_{CPD}) between the probe tip and the sample surface.

$$V_{CPD} = \frac{\Phi_{tip} - \Phi_{sample}}{e} \quad (1)$$

https://doi.org/10.1021/acs.jpcc.2c09122
J. Phys. Chem. C 2023, 127, 7461−7470

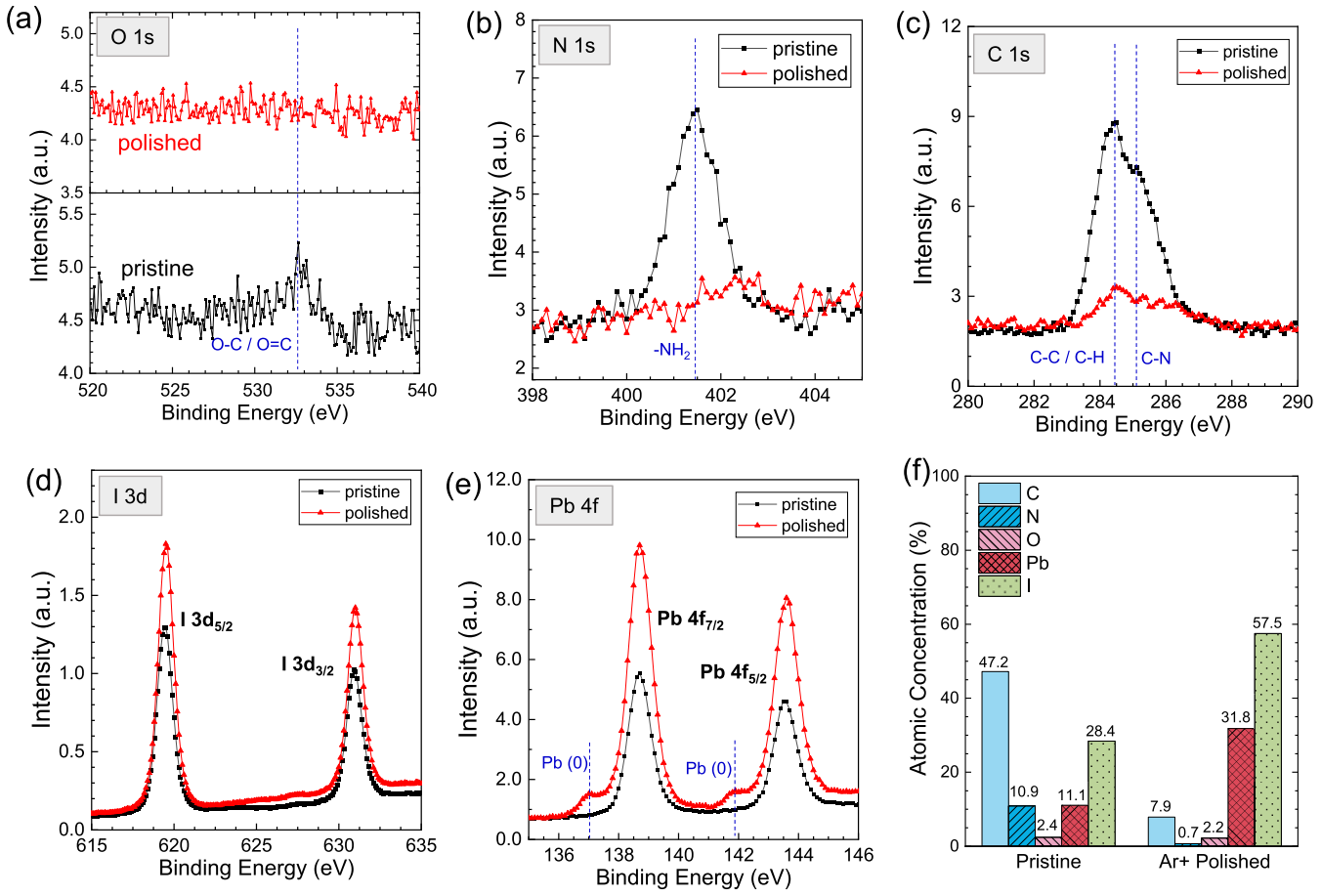

Figure 4. High-resolution XPS profiles of pristine (black lines) and polished (red lines) samples. Significant decreases of the organic compositions are seen with the Ar^+-polished sample: (a) O 1s, (b) N 1s, and (c) C 1s. XPS signatures of (d) iodine (I $3d_{3/2}$ and I $3d_{5/2}$) and (f) lead (Pb $4f_{5/2}$ and Pb $4f_{7/2}$) increase with the polishing. The additional peaks near the shoulders of the Pb 4f doublet peaks infer the introduction of metallic lead [Pb (0); 137.1 and 142 eV] and oxidized lead [Pb (II); 138.7 and 143.6 eV] under Ar^+ beam irradiation. (f) Summary of the atomic percentage of $MAPbI_3$ "before (pristine)" and "after (polished)" the ion beam irradiation. An estimated statistical error of XPS is ±5%.

Here, Φ_{sample} is the work function of $MAPbI_3$, Φ_{tip} is the work function of the probe tip, and e is the elementary charge (1.6×10^{-19} C).[28] In our measurements, a probe tip (Pt/Ir-coated Si cantilever) was raster scanned on $MAPbI_3$ at a scan rate of 0.5 Hz in a tapping mode under an ambient environment, while the FTO layer of the sample was connected to ground via conductive Ag paste. Topography and the CPD raw datasets were simultaneously recorded. The grain size of pristine $MAPbI_3$ ranges from 100's nm to ≈1 μm, and the peak-to-valley roughness is approximately ≈100 nm (Figure 3a). As seen in Figure 3b, this surface roughness notably reduces to 10's nm after polishing it with an Ar^+ beam (4 kV irradiated at 3° for ten minutes). The topography of the milled sample presents porous structures and pinholes, primarily near grain boundaries. This porosity is likely attributed to the grain growth during the thermal annealing after spin-coating of PSC precursors.[22] Figure 3c,d displays the corresponding CPD distribution of the pristine and polished samples, showing relatively uniform surface potentials rather than distinct electronic structures at individual microstructures. A careful KPFM study by Lanzoni et al. found that an apparent CPD contrast of $MAPbI_3$ microstructures became weaker under an ambient condition than in a vacuum when measuring the same sample.[29] Our low CPD contrast indicates possible partial oxidation at the surface. While performing KPFM characterization under ambient conditions results in a loss of facet-related surface potential contrast associated with air exposure,[29] the primary focus of KPFM characterization was observing average surface potential changes associated with ion beam exposure. As such, the average CPD value for Ar^+ beam exposed and unexposed samples was measured to determine the net surface potential change associated with Ar ion exposure. Identical air exposure of samples during KPFM characterization was maintained as a control to isolate the variation of the CPD associated with ion-beam exposure. For a quantitative comparison, we determine the work function of $MAPbI_3$ from eq 1. The mean V_{CPD} values of the pristine and the polished samples are approximately −179 and 328 mV, respectively, calculated from the CPD maps in Figure 3c,d. The work function of the probe tip, $\Phi_{tip} \approx 4.24$ eV ± 0.15 eV, was first calibrated by measuring the CPD between the atomic force microscopy (AFM) probe and standard references of the Au ($\Phi_{Au} \approx 4.6$ eV) film and HOPG ($\Phi_{HOPG} \approx 5.1$ eV).[30] Based upon the calibrated work function of the AFM probe, we calculate a work function of approximately 3.91 eV ± 0.15 eV for pristine $MAPbI_3$ (glass/FTO/SnO_2/$MAPbI_3$). This estimation reasonably agrees with the reported work function.[31] The notable CPD reduction after the polishing ($\Delta V_{CPD} \approx 510$ mV) suggests that the irradiating Ar^+ beam can further impact the electronic structures of the $MAPbI_3$ (sub)surface more than partial oxidation in air exposure.

To directly probe the elemental changes of $MAPbI_3$ responsible for the observed PL and KPFM, we carry out XPS.

https://doi.org/10.1021/acs.jpcc.2c09122
J. Phys. Chem. C 2023, 127, 7461−7470

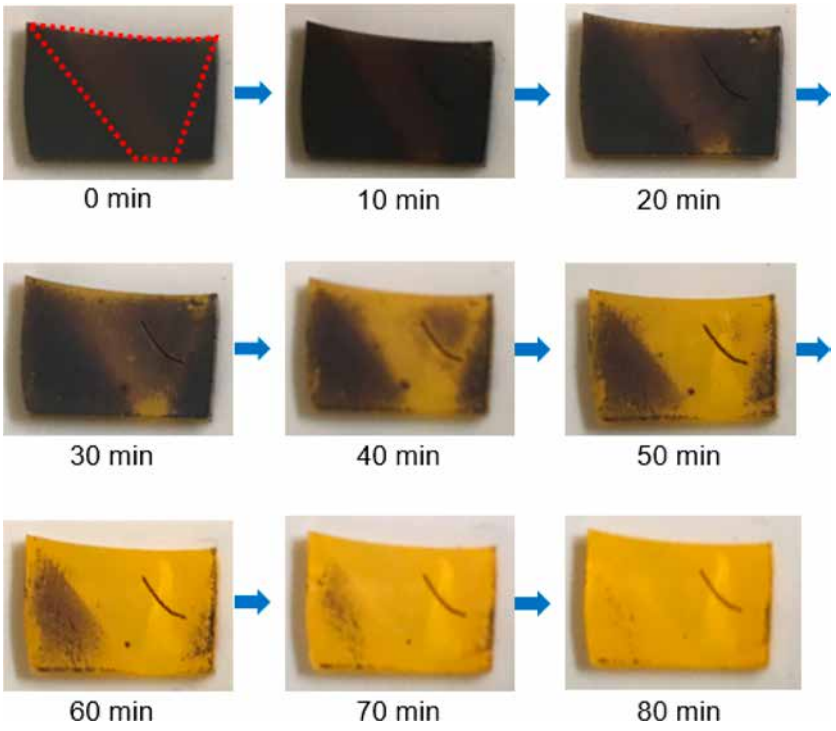

Figure 5. Series of photographs of $MAPbI_3$ taken during thermal aging at 150 °C. The Ar^+-polished region (4 kV Ar^+ beam injected at an angle of 3°) is marked by red dotted lines. Insignificant color changes are observed for the first 10 min. At ≈20 min, visible yellow spots are seen near the edge of the ion-beam exposed area, continuously expanding to the entire polished region (trapezoidal zone) with time. An apparent color change of the unpolished zones is seen after ≈50 min heating. At ≈80 min, the color of the entire sample was turned from dark brown ($MAPbI_3$) into vivid yellow (PbI_2), indicating complete compositional dissociation.

At a nominal beam spot size of 300 μm × 700 μm, XPS resolves the local chemical information near the surface (<10 nm). The survey spectra acquired on a pristine and a polished sample are shown in Figure S3. Beginning with a pristine sample, the peaks of organic elements of C 1s, N 1s, and O 1s are observed near 285, 402, and 533 eV, respectively. Four core level peaks of inorganic atoms are also apparent for this pristine sample: I 4d (40−60 eV), Pb 4f (130−150 eV), Pb 4d (410−450 eV), and I 3d (610−650 eV).[32,33] After the ion beam exposure, the XPS peaks of the organic components are significantly reduced or almost diminished, while the inorganic atoms (Pb and I) show strong peaks.

To gain a better understanding, we perform an in-depth analysis using high-resolution XPS profiles. Figure 4a compares the core-level O 1s spectra of the samples. While relatively weak, the O 1s signal of the pristine control indicates partial oxidation of the surface, evidence of the low CPD contrast of microstructures observed in KPFM (Figure 3c). The O 1s signature near 533 eV and the N 1s peak near 401.5 eV (Figure 4b) almost vanished after Ar^+ milling. Figure 4c shows the core-level 1s spectra of C. This broad C 1s peak contains convoluted signatures of C−C, C−H, and C−N bonding.[34] The significantly reduced peak intensity indicates that the ionized Ar atoms physically remove the lighter elements (i.e., C and N) at the surface. While the air exposure of the Ar^+-polished $MAPbI_3$ was limited during the sample transport to XPS, the dangling bonds of C 1s can be susceptible to forming COO− bonds in ambient air, accelerating the chemical deterioration of $MAPbI_3$ observed in the following heating experiments.

On the other hand, the inorganic components (I and Pb) show noticeably enhanced XPS signals. The peaks of the doublet states of I 3d (619.5 and 631 eV; Figure 4d) and Pb 4f (138.5, 143.5 eV; Figure 4e) substantially increase with Ar^+ milling. Interestingly, the Pb 4f spectrum of the polished sample shows the additional new peaks near the shoulders of the Pb 4f doublet peaks (blue dotted lines in Figure 4e). We decompose the peaks using a Gaussian−Lorentz model, confirming the new peaks of metallic lead [Pb (0); 137.1 and 142 eV] and oxidized lead [Pb (II); 138.7 and 143.6 eV].[34,35] As Rajendra Kumar et al. suggested, the presence of the unsaturated Pb defects in the $MAPbI_3$ lattice can further oxidize it to lead monoxide (PbO) under thermal aging processes.[34] In Figure 4f, we show a summary of the compositional changes after Ar ion polishing. The overall I/Pb ratio decreases from 2.6 of pristine to 2.1 with polishing, implying the $MAPbI_3$ surface may be partially decomposed to lead iodide (PbI_2) or their complexes. Our XPS analysis suggests that the ion beam irradiation alters the atomic structure of the surface, and the locally damaged subsurface resulting from broken bonds can further affect phase segregation and degradation of $MAPbI_3$ under aging processes.

We qualitatively examine how the modified $MAPbI_3$ surface under ion beams influences bulk deterioration under a heat stressor. A separate sample with a geometry illustrated in Figure 1 was prepared by Ar^+ milling (i.e., a 4 kV Ar^+ beam injected at an angle of 3° parallel to the sample surface). By setting the beam focus of 0%, the ion beam propagates on the sample surface in a trapezoidal shape (marked by red dotted lines) while preserving unirradiated areas on the sample. A heat lamp facing the polished sample surface was placed above a sample stage, maintaining the sample temperature of 150 °C. Figure 5 shows a series of sample images taken at different times. We observe an insignificant color change for the first 10 min. At ≈20 min, visible yellow spots are seen near the edge of the ion-beam-exposed area, which is continuously expanding to the entire

https://doi.org/10.1021/acs.jpcc.2c09122
J. Phys. Chem. C 2023, 127, 7461−7470

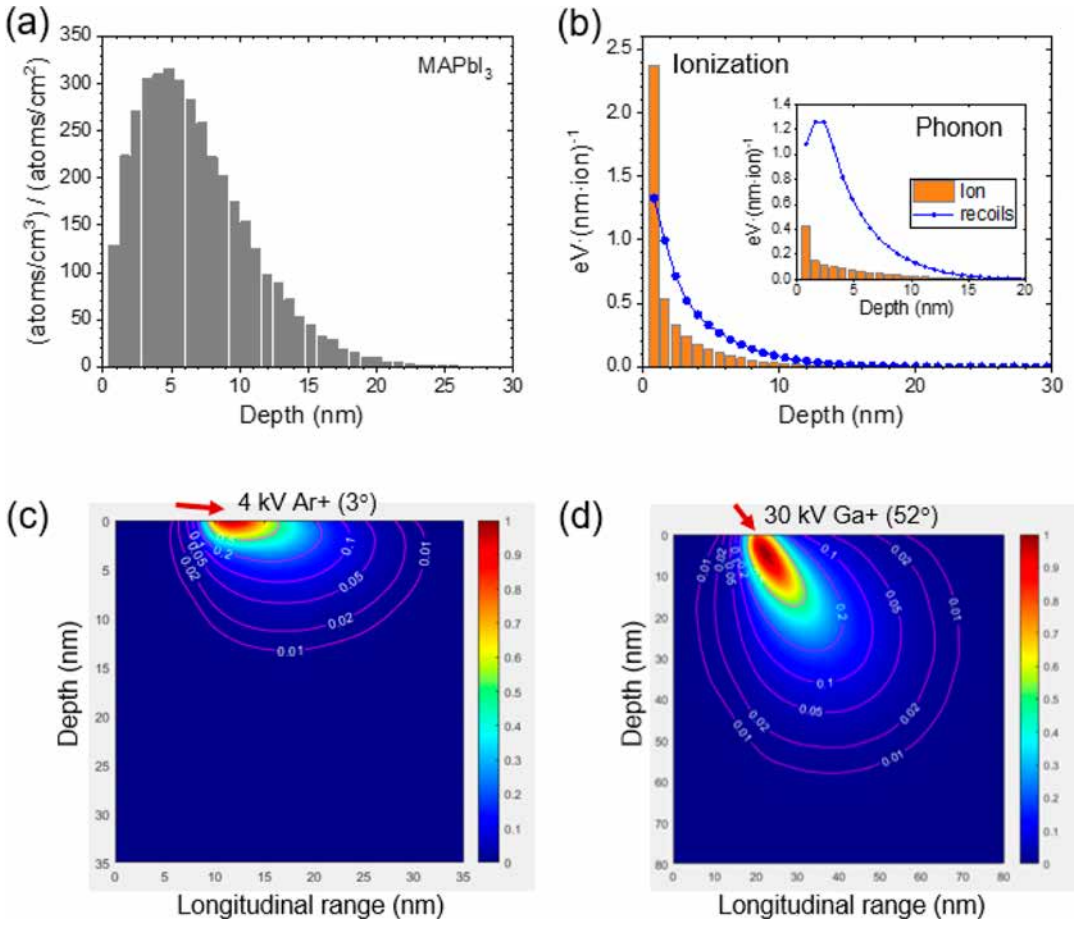

Figure 6. SRIM/TRIM simulations estimate the ion beam damage in $MAPbI_3$. (a) Distribution of the total ion range in $MAPbI_3$. (b) Plots showing the ionization profiles of the primary Ar^+ ions and their recoils. The inset displays the energy loss of the primary ions and the recoils to phonons. (c) Contour plots showing the distribution of the total atomic displacement by a (c) 4 kV Ar^+ ion at 3° and a (d) 30 kV Ga^+ ion at 52° irradiated onto the $MAPbI_3$ surface. The simulations predict a damage layer of ≈15 nm for the Ar^+ beam and ≈60 nm for the Ga^+ beam.

polished region (trapezoidal zone) with time. An apparent color change of the unpolished zones is seen after ≈50 min of heating. At ≈80 min, the color of the entire sample was turned from dark brown ($MAPbI_3$) into vivid yellow (PbI_2), indicating complete compositional dissociation. Our observation is consistent with the previous studies demonstrating an irreversible chemical dissociation of $MAPbI_3$ into PbI_2 at around 150 to 200 °C.[36] It is not surprising to observe the fast-thermal degradation on the ion-beam exposed area due to initial compositional alteration during the Ar^+ milling. However, we observe notably different degradation speeds, where the unexposed areas show marginal color changes (≈40 min) until the entire area exposed to the Ar^+ beam is segregated into PbI_2. Previous studies suggest that the defect states at the surface and interfaces play a more significant role than point defects in bulk in their degradation mechanisms.[37,38] Our preliminary experiment supports the sensitivity of the surface and interface states of metal-halide perovskites in thermal aging processes.

To elucidate the detailed dynamics of the ion beam with perovskites, we simulate atomic displacements in $MAPbI_3$ by Ar^+ beams using SRIM and TRIM. This program package is built on the fundamental knowledge about atomic interaction, collisions, and transport theory, frequently used for calculating the damage profile and implanted ion range of various materials.[39,40] SRIM calculates the electronic stopping power by fitting experimental data, whereas TRIM simulates the energy loss of the incident atom to target electrons and the knock-on atoms along the ion path in the material. In our full cascade model, 200,000 Ar atoms at 4 kV were injected at an incident angle of 3° parallel to the surface of $MAPbI_3$ (Figure 1). The standard data in the program set the material parameters of Ar and $MAPbI_3$ (e.g., atomic weight, displacement energy, lattice energy, surface energy, etc.) except for the mass density of $MAPbI_3$ (4.16 g/cm^3), which was obtained from the literature.[41]

Figure 6 displays the estimated damage distribution in $MAPbI_3$ caused by the Ar ion beam. As seen in Figure 6a, the injected 4 kV Ar ions penetrate $MAPbI_3$ as high as 25 nm. The energy loss of the ions and their recoils occurs near the surface (5 nm), causing irreversible ionization. Figure 6b shows that part of the energy loss can contribute to the lattice vibration, primarily attributed to the recoils (Figure 6b). The calculated total energy loss is distributed into ionization of ≈47%, vacancies of ≈6%, and phonons of ≈47%. Taken together, we estimate the total atomic displacement of an approximately 15 nm thick subsurface of $MAPbI_3$, where over 90% of the damage is mainly concentrated within a 5 nm subsurface. For comparison, we simulate the beam damage in $MAPbI_3$ under typical Ga^+ FIB processes (30 kV irradiation at an incident angle of 52°). The damage cascade is displayed in an elongated pear shape with the central axis along the trajectory of the primary Ar ions (Figure 6). The estimated atomic displacement ranges over 50 nm in the depth of $MAPbI_3$, suggesting that post-polishing processes are

https://doi.org/10.1021/acs.jpcc.2c09122
J. Phys. Chem. C 2023, 127, 7461−7470

necessary before high-resolution microscopy measurements. The contour plots in Figure 6c,d summarize the distribution profiles for both cases.

The simulation results provide useful insight into beam damage profiles in metal-halide perovskites that can be correlated to the observed subsurface characteristics. For instance, the PL intensities after Ar^+ milling drop by about 40% compared to the unexposed areas (Figure 2). Considering the spontaneous photoluminescence to be proportional to the absorption profile,[42] we estimate that approximately 40% of the total PL emission is attributed to the 15 nm-thick surfaces of $MAPbI_3$ under a 244 nm laser beam illumination (Figure S1). It appears that the Ar^+ milling introduces atomic displacement (e.g., local disorder and point defects), resulting in an optically inactive "dead layer". On the other hand, TRIM calculates that approximately 47% of the total energy loss is transferred to the phonon energy in the subsurface. This immense energy deposition in the subsurface of $MAPbI_3$ with relatively low thermal conductivity (≈0.3 W/m K)[43] can substantially increase the local temperature above 200 °C.[44−46] This agrees with the XPS experimental results, where the signature of the presence of PbI_2 and its complexes is apparent in the polished sample (Figure 6b).

4. SUMMARY AND CONCLUSIONS

In summary, we examine the effects of ion beam exposure on metal-halide perovskites by measuring the subsurface characteristics. We find that the irradiation lowers the band gap PL emission in $MAPbI_3$ by 40% while increasing the surface potential. Several signatures of the chemical modification are observed at the $MAPbI_3$ surface. XPS analysis shows that the peak of the organic components (e.g., C and N) diminishes over 80% while enhancing inorganic signatures (e.g., Pb, I) over 200% after the beam exposure. The comparison of atomic concentrations suggests that Ar^+ milling introduces a lead-rich, iodine-deficient $MAPbI_3$ surface. Our experiments, together with SRIM/TRIM simulations, suggest that the presence of PbI_2 and the complexes on the subsurface is associated with the "dead layer" introduced by the ion beam via atomic displacement and local heating. Specifically, an approximately 15 nm thick subsurface of $MAPbI_3$ can be damaged by a 4 kV Ar^+ beam irradiated at an incident angle of 3°. Our findings convey that the practical use of ion beams requires care for perovskite measurements under accelerated stressors. The thickness of the "dead layer" can be reduced by mitigating the local heating (e.g., a cryogenic sample stage) and the kinetic beam energy (e.g., a low beam voltage). Despite the subsurface modification, our work supports that the rest of the $MAPbI_3$ bulk retains the properties, as observed in PL. This implies that FIB-prepared perovskite samples could serve in studying the properties of bulk or buried junctions far away from the altered subsurface. Such surface-insensitive measurement approaches include two-photon PL and micro LBIC (laser beam-induced current), where the wavelengths of the laser beams can tune the profiles of photon absorption and excess carrier generations.

■ ASSOCIATED CONTENT

Supporting Information

The Supporting Information is available free of charge at https://pubs.acs.org/doi/10.1021/acs.jpcc.2c09122.

FDTD simulations and XPS survey spectra (PDF)

■ AUTHOR INFORMATION

Corresponding Author

Heayoung P. Yoon − *Department of Electrical and Computer Engineering and Department of Materials Science and Engineering, University of Utah, Salt Lake City, Utah 84112, United States;* orcid.org/0000-0003-0321-5288; Email: heayoung.yoon@utah.edu

Authors

Yu-Lin Hsu − *Department of Electrical and Computer Engineering, University of Utah, Salt Lake City, Utah 84112, United States*

Chongwen Li − *Department of Physics and Astronomy and Wright Center for Photovoltaics Innovation and Commercialization, The University of Toledo, Toledo, Ohio 43606, United States*

Andrew C. Jones − *Center for Integrated Nanotechnologies, Materials Physics and Applications Division, Los Alamos National Laboratory, Los Alamos, New Mexico 87545, United States;* orcid.org/0000-0001-9205-4847

Michael T. Pettes − *Center for Integrated Nanotechnologies, Materials Physics and Applications Division, Los Alamos National Laboratory, Los Alamos, New Mexico 87545, United States;* orcid.org/0000-0001-6862-6841

Ashif Chowdhury − *Department of Electrical and Computer Engineering, University of Utah, Salt Lake City, Utah 84112, United States*

Yanfa Yan − *Department of Physics and Astronomy and Wright Center for Photovoltaics Innovation and Commercialization, The University of Toledo, Toledo, Ohio 43606, United States;* orcid.org/0000-0003-3977-5789

Complete contact information is available at: https://pubs.acs.org/10.1021/acs.jpcc.2c09122

Notes

The authors declare no competing financial interest.

■ ACKNOWLEDGMENTS

The authors thank K. Powell and P. Perez for valuable discussions and assisting with the analysis during this work. This research was supported by the U.S. Department of Energy's Office of Energy Efficiency and Renewable Energy (EERE) under the DE-FOA-0002064 program award number DE-EE0008985. This work was performed, in part, at the Center for Integrated Nanotechnologies, an Office of Science User Facility operated for the U.S. Department of Energy's (DOE) Office of Science. The Los Alamos National Laboratory, an affirmative action equal opportunity employer, is managed by Triad National Security, LLC, for the U.S. Department of Energy's NNSA, under contract 89233218CNA000001. M.P. acknowledges support from the Laboratory-Directed Research and Development (LDRD) award 20210640ECR. Y.Y. acknowledges the support of NSF under award no. DMR-1807818. This work was supported by the USTAR shared facilities at the University of Utah, in part, by the MRSEC Program of NSF under the award no. DMR-1121252. H.Y. acknowledges the support from the NSF CAREER award no. 2048152.

■ REFERENCES

(1) Giannuzzi, L. A.; Stevie, F. A. A review of focused ion beam milling techniques for TEM specimen preparation. *Micron* **1999**, *30*, 197−204.

(2) Huang, Z. Combining Ar ion milling with FIB lift-out techniques to prepare high quality site-specific TEM samples. *J. Microsc.* **2004**, *215*, 219−223.
(3) Kim, C.-S.; Ahn, S.-H.; Jang, D.-Y. Review: Developments in micro/nanoscale fabrication by focused ion beams. *Vacuum* **2012**, *86*, 1014−1035.
(4) Giannuzzi, L. A.; Stevie, F. A. *Introduction to focused ion beams : instrumentation, theory, techniques, and practice*; Springer: New York, 2005.
(5) Bischoff, L.; Mazarov, P.; Bruchhaus, L.; Gierak, J. Liquid metal alloy ion sources—An alternative for focussed ion beam technology. *Appl. Phys. Rev.* **2016**, *3*, 021101.
(6) Kato, N. I. Reducing focused ion beam damage to transmission electron microscopy samples. *J. Electron Microsc.* **2004**, *53*, 451−458.
(7) Turner, E. M.; Sapkota, K. R.; Hatem, C.; Lu, P.; Wang, G. T.; Jones, K. S. Wet-chemical etching of FIB lift-out TEM lamellae for damage-free analysis of 3-D nanostructures. *Ultramicroscopy* **2020**, *216*, 113049.
(8) Campin, M. J.; Bonifacio, C. S.; Nowakowski, P.; Fischione, P. E.; Giannuzzi, L. A. Narrow-Beam Argon Ion Milling of Ex Situ Lift-Out FIB Specimens Mounted on Various Carbon-Supported Grids. *International Symposium for Testing and Failure Analysis 2018*; ASM International, 2018; pp 339−344.
(9) Meng, X.; Tian, X.; Zhang, S.; Zhou, J.; Zhang, Y.; Liu, Z.; Chen, W. In Situ Characterization for Understanding the Degradation in Perovskite Solar Cells. *Sol. RRL* **2022**, *6*, 2200280.
(10) Ran, J.; Dyck, O.; Wang, X.; Yang, B.; Geohegan, D. B.; Xiao, K. Electron-Beam-Related Studies of Halide Perovskites: Challenges and Opportunities. *Adv. Energy Mater.* **2020**, *10*, 1903191.
(11) Di Girolamo, D.; Phung, N.; Kosasih, F. U.; Di Giacomo, F.; Matteocci, F.; Smith, J. A.; Flatken, M. A.; Köbler, H.; Turren Cruz, S. H.; Mattoni, A.; et al. Ion Migration-Induced Amorphization and Phase Segregation as a Degradation Mechanism in Planar Perovskite Solar Cells. *Adv. Energy Mater.* **2020**, *10*, 2000310.
(12) Seo, Y.-H.; Kim, J. H.; Kim, D.-H.; Chung, H.-S.; Na, S.-I. In situ TEM observation of the heat−induced degradation of single− and triple−cation planar perovskite solar cells. *Nano Energy* **2020**, *77*, 105164.
(13) Byeon, J.; Kim, J.; Kim, J.-Y.; Lee, G.; Bang, K.; Ahn, N.; Choi, M. Charge transport layer-dependent electronic band bending in perovskite solar cells and its correlation to light-induced device degradation. *ACS Energy Lett.* **2020**, *5*, 2580−2589.
(14) Zhao, Y.; Zhou, W.; Han, Z.; Yu, D.; Zhao, Q. Effects of ion migration and improvement strategies for the operational stability of perovskite solar cells. *Phys. Chem. Chem. Phys.* **2021**, *23*, 94−106.
(15) Chen, S.; Zhang, Y.; Zhao, J.; Mi, Z.; Zhang, J.; Cao, J.; Feng, J.; Zhang, G.; Qi, J.; Li, J.; Gao, P. Transmission electron microscopy of organic-inorganic hybrid perovskites: myths and truths. *Sci. Bull.* **2020**, *65*, 1643−1649.
(16) Deng, Y.-H. Perovskite decomposition and missing crystal planes in HRTEM. *Nature* **2021**, *594*, E6−E7.
(17) Xiao, C. X.; Li, Z.; Guthrey, H.; Moseley, J.; Yang, Y.; Wozny, S.; Moutinho, H.; To, B.; Berry, J. J.; Gorman, B.; et al. Mechanisms of Electron-Beam-Induced Damage in Perovskite Thin Films Revealed by Cathodoluminescence Spectroscopy. *J. Phys. Chem. C* **2015**, *119*, 26904−26911.
(18) Miyazawa, Y.; Ikegami, M.; Chen, H. W.; Ohshima, T.; Imaizumi, M.; Hirose, K.; Miyasaka, T. Tolerance of Perovskite Solar Cell to High-Energy Particle Irradiations in Space Environment. *Iscience* **2018**, *3*, 86.
(19) Kosasih, F. U.; Divitini, G.; Orri, J. F.; Tennyson, E. M.; Kusch, G.; Oliver, R. A.; Stranks, S. D.; Ducati, C. Optical emission from focused ion beam milled halide perovskite device cross-sections. *Microsc. Res. Tech.* **2022**, *85*, 2351−2355.
(20) Wang, C.; Xiao, C.; Yu, Y.; Zhao, D.; Awni, R. A.; Grice, C. R.; Ghimire, K.; Constantinou, I.; Liao, W.; Cimaroli, A. J.; et al. Understanding and Eliminating Hysteresis for Highly Efficient Planar Perovskite Solar Cells. *Adv. Energy Mater.* **2017**, *7*, 1700414.
(21) Stoumpos, C. C.; Malliakas, C. D.; Kanatzidis, M. G. Semiconducting Tin and Lead Iodide Perovskites with Organic Cations: Phase Transitions, High Mobilities, and Near-Infrared Photoluminescent Properties. *Inorg. Chem.* **2013**, *52*, 9019−9038.
(22) Zhou, Y.; Yang, M.; Vasiliev, A. L.; Garces, H. F.; Zhao, Y.; Wang, D.; Pang, S.; Zhu, K.; Padture, N. P. Growth control of compact CH3NH3PbI3 thin films via enhanced solid-state precursor reaction for efficient planar perovskite solar cells. *J. Mater. Chem. A* **2015**, *3*, 9249−9256.
(23) Ghimire, K.; Zhao, D.; Cimaroli, A.; Ke, W.; Yan, Y.; Podraza, N. J. Optical monitoring of CH3NH3PbI3 thin films upon atmospheric exposure. *J. Phys. D: Appl. Phys.* **2016**, *49*, 405102.
(24) Lumerical computation solutions. https://www.lumerical.com/ (accessed October, 2022).
(25) Shirayama, M.; Kadowaki, H.; Miyadera, T.; Sugita, T.; Tamakoshi, M.; Kato, M.; Fujiseki, T.; Murata, D.; Hara, S.; Murakami, T. N.; et al. Optical Transitions in Hybrid Perovskite Solar Cells: Ellipsometry, Density Functional Theory, and Quantum Efficiency Analyses for CH3NH3PbI3. *Phys. Rev. Appl.* **2016**, *5*, 014012.
(26) Alvarado-Leaños, A. L.; Cortecchia, D.; Folpini, G.; Srimath Kandada, A. R.; Petrozza, A. Optical Gain of Lead Halide Perovskites Measured via the Variable Stripe Length Method: What We Can Learn and How to Avoid Pitfalls. *Adv. Opt. Mater.* **2021**, *9*, 2001773.
(27) Chen, X.; Xia, Y.; Huang, Q.; Li, Z.; Mei, A.; Hu, Y.; Wang, T.; Cheacharoen, R.; Rong, Y.; Han, H. Tailoring the Dimensionality of Hybrid Perovskites in Mesoporous Carbon Electrodes for Type-II Band Alignment and Enhanced Performance of Printable Hole-Conductor-Free Perovskite Solar Cells. *Adv. Energy Mater.* **2021**, *11*, 2100292.
(28) Chandra Shakher, P. Application of Atomic Force Microscopy in Organic and Perovskite Photovoltaics. *Recent Developments in Atomic Force Microscopy and Raman Spectroscopy for Materials Characterization*; Chandra Shakher, P., Samir, K., Eds.; IntechOpen: Rijeka, 2021; Ch. 1.
(29) Lanzoni, E. M.; Gallet, T.; Spindler, C.; Ramirez, O.; Boumenou, C. K.; Siebentritt, S.; Redinger, A. The impact of Kelvin probe force microscopy operation modes and environment on grain boundary band bending in perovskite and Cu(In,Ga)Se2 solar cells. *Nano Energy* **2021**, *88*, 106270.
(30) Panchal, V.; Pearce, R.; Yakimova, R.; Tzalenchuk, A.; Kazakova, O. Standardization of surface potential measurements of graphene domains. *Sci. Rep.* **2013**, *3*, 2597.
(31) Gallet, T.; Lanzoni, E. M.; Redinger, A. Effects of Annealing and Light on Co-evaporated Methylammonium Lead Iodide Perovskites using Kelvin Probe Force Microscopy in Ultra-High Vacuum. *2019 IEEE 46th Photovoltaic Specialists Conference (PVSC), 2019/06/16/21*; Institute of Electrical and Electronics Engineers, 2019; pp 1477−1482.
(32) Olthof, S.; Meerholz, K. Substrate-dependent electronic structure and film formation of MAPbI3 perovskites. *Sci. Rep.* **2017**, *7*, 40267.
(33) Guo, X.; McCleese, C.; Kolodziej, C.; Samia, A. C. S.; Zhao, Y.; Burda, C. Identification and characterization of the intermediate phase in hybrid organic−inorganic MAPbI3 perovskite. *Dalton Trans.* **2016**, *45*, 3806−3813.
(34) Rajendra Kumar, G.; Dennyson Savariraj, A.; Karthick, S. N.; Selvam, S.; Balamuralitharan, B.; Kim, H.-J.; Viswanathan, K. K.; Vijaykumar, M.; Prabakar, K. Phase transition kinetics and surface binding states of methylammonium lead iodide perovskite. *Phys. Chem. Chem. Phys.* **2016**, *18*, 7284−7292.
(35) Lin, W.-C.; Lo, W.-C.; Li, J.-X.; Wang, Y.-K.; Tang, J.-F.; Fong, Z.-Y. In situ XPS investigation of the X-ray-triggered decomposition of perovskites in ultrahigh vacuum condition. *npj Mater. Degrad.* **2021**, *5*, 13.
(36) Kim, T. W.; Shibayama, N.; Cojocaru, L.; Uchida, S.; Kondo, T.; Segawa, H. Real-Time In Situ Observation of Microstructural Change in Organometal Halide Perovskite Induced by Thermal Degradation. *Adv. Funct. Mater.* **2018**, *28*, 1804039.
(37) Kim, N.-K.; Min, Y. H.; Noh, S.; Cho, E.; Jeong, G.; Joo, M.; Ahn, S.-W.; Lee, J. S.; Kim, S.; Ihm, K.; et al. Investigation of Thermally Induced Degradation in CH3NH3PbI3 Perovskite Solar Cells using In-situ Synchrotron Radiation Analysis. *Sci. Rep.* **2017**, *7*, 4645.

https://doi.org/10.1021/acs.jpcc.2c09122
J. Phys. Chem. C 2023, 127, 7461−7470

(38) Dunfield, S. P.; Bliss, L.; Zhang, F.; Luther, J. M.; Zhu, K.; Hest, M. F. A. M.; Reese, M. O.; Berry, J. J. From Defects to Degradation: A Mechanistic Understanding of Degradation in Perovskite Solar Cell Devices and Modules. *Adv. Energy Mater.* **2020**, *10*, 1904054.
(39) Ziegler, J. F.; Ziegler, M. D.; Biersack, J. P. SRIM—The stopping and range of ions in matter 2010. *19th International Conference on Ion Beam Analysis*; Elsevier, 2010; Vol. *268*, pp 1818−1823.
(40) Luo, P.; Sun, X.-Y.; Li, Y.; Yang, L.; Shao, W.-Z.; Zhen, L.; Xu, C.-Y. Correlation between Structural Evolution and Device Performance of CH3NH3PbI3 Solar Cells under Proton Irradiation. *ACS Appl. Energy Mater.* **2021**, *4*, 13504−13515.
(41) Stuckelberger, M.; Nietzold, T.; Hall, G. N.; West, B.; Werner, J.; Niesen, B.; Ballif, C.; Rose, V.; Fenning, D. P.; Bertoni, M. I. Elemental distribution and charge collection at the nanoscale on perovskite solar cells. *2016 IEEE 43rd Photovoltaic Specialists Conference (PVSC), 2016/06/05/10*; Institute of Electrical and Electronics Engineers, 2016; pp 1191−1196.
(42) van Roosbroeck, W.; Shockley, W. Photon-Radiative Recombination of Electrons and Holes in Germanium. *Phys. Rev.* **1954**, *94*, 1558−1560.
(43) Heiderhoff, R.; Haeger, T.; Pourdavoud, N.; Hu, T.; Al-Khafaji, M.; Mayer, A.; Chen, Y.; Scheer, H.-C.; Riedl, T. Thermal Conductivity of Methylammonium Lead Halide Perovskite Single Crystals and Thin Films: A Comparative Study. *J. Phys. Chem. C* **2017**, *121*, 28306−28311.
(44) Süess, M. J.; Mueller, E.; Wepf, R. Minimization of amorphous layer in Ar+ ion milling for UHR-EM. *Ultramicroscopy* **2011**, *111*, 1224−1232.
(45) Barber, D. J. Radiation damage in ion-milled specimens: characteristics, effects and methods of damage limitation. *Ultramicroscopy* **1993**, *52*, 101−125.
(46) Park, Y. M.; Ko, D.-S.; Yi, K.-W.; Petrov, I.; Kim, Y.-W. Measurement and estimation of temperature rise in TEM sample during ion milling. *Ultramicroscopy* **2007**, *107*, 663−668.

https://doi.org/10.1021/acs.jpcc.2c09122
J. Phys. Chem. C 2023, 127, 7461−7470